Using 915 nm Laser Excited Tm^{3+}/Er^{3+}/Ho^{3+}-Doped NaYbF4 Upconversion Nanoparticles for *in Vitro* and Deeper *in Vivo* Bioimaging without Overheating Irradiation

Qiuqiang Zhan,[†,‡,∥] Jun Qian,[†,∥] Huijuan Liang,[§] Gabriel Somesfalean,[†,§,⊥] Dan Wang,[†] Sailing He,[†,‡,*] Zhiguo Zhang,[§] and Stefan Andersson-Engels[⊥]

[†]Centre for Optical and Electromagnetic Research, State Key Laboratory of Modern Optical Instrumentations, JORCEP [Joint Research Center of Photonics of the Royal Institute of Technology (Sweden), Lund University (Sweden), and Zhejiang University], Zhejiang University, Zhijingang Campus, 310058 Hangzhou, China, [‡]ZJU-SCNU Joint Research Center of Photonics, South China Normal University, 510006 Guangzhou, China, [§]Department of Physics, Harbin Institute of Technology, 150001 Harbin, China, and [⊥]Department of Physics, Lund University, P.O. Box 118, 22100 Lund, Sweden. [∥]These authors contributed equally to this work.

ABSTRACT Successful further development of superhigh-constrast upconversion (UC) bioimaging requires addressing the existing paradox: 980 nm laser light is used to excite upconversion nanoparticles (UCNPs), while 980 nm light has strong optical absorption of water and biological specimens. The overheating caused by 980 nm excitation laser light in UC bioimaging is computationally and experimentally investigated for the first time. A new promising excitation approach for better near-infrared to near-infrared (NIR-to-NIR) UC photoluminescence *in vitro* or *in vivo* imaging is proposed employing a cost-effective 915 nm laser. This novel laser excitation method provides drastically less heating of the biological specimen and larger imaging depth in the animals or tissues due to quite low water absorption. Experimentally obtained thermal-graphic maps of the mouse in response to the laser heating are investigated to demonstrate the less heating advantage of the 915 nm laser. Our tissue phantom experiments and simulations verified that the 915 nm laser is superior to the 980 nm laser for deep tissue imaging. A novel and facile strategy for surface functionalization is utilized to render UCNPs hydrophilic, stable, and cell targeting. These as-prepared UCNPs were characterized by TEM, emission spectroscopy, XRD, FTIR, and zeta potential. Specifically targeting UCNPs excited with a 915 nm laser have shown very high contrast UC bioimaging. Highly stable DSPE-mPEG-5000-encapsulated UCNPs were injected into mice to perform *in vivo* imaging. Imaging and spectroscopy analysis of UC photoluminescence demonstrated that a 915 nm laser can serve as a new promising excitation light for UC animal imaging.

KEYWORDS: upconversion nanoparticles · bioimaging · deep imaging · overheating free · near-infrared

Photoluminescence imaging using nanoparticles is a powerful tool for biological studies and clinical medical applications due to its high resolution and sensitivity.[1−5] On the basis of downconverting photoluminescence, these traditional fluophors normally emit a lower energy photon when excited by a higher energy photon.[6] Using high-energy excitation photons always has serious drawbacks: significant autofluorescence from biological samples resulting in low signal-to-background ratio and considerable absorption and scattering effects for visible light, inducing short penetration depth in biological tissues. The near-infrared (NIR) light allows deeper penetration depth for *in vivo* bioimaging and can efficiently suppress autofluorescence and light scattering.[7,8] Nanoparticles doped with NIR light absorbing organic fluophors can be excited in the NIR range using single-photon excitation with NIR emission.[9,10] Unfortunately those organic dyes often suffer from intrinsic photobleaching deficiency and low emission efficiency.[11−13] NIR quantum dots (QDs) have recently been synthesized and used in many studies and are more stable against photobleaching than organic fluophors.[14,15] However, due to the fact that typical QDs are composed of heavy metals (*e.g.*, CdSe) and can easily penetrate into cells, there is a wide and persistent concern about the toxicity of QDs, even though much work is underway to synthesize less harmful QDs or enhance their biocompatibility.[16,17]

Superior to organic dyes and QDs, upconversion nanophosphors (UCNPs) can emit anti-Stokes-shifted light after being excited by NIR (900−1000 nm) continuous-wave (CW) laser light. UCNP is a kind of nanocrystal co-doped with several trivalent rare earth ions. As the most efficient host material, $NaYF_4$ nanoparticles are typically co-doped with Yb^{3+} (as sensitizer) and another ion (*e.g.*, Tm^{3+}, Er^{3+}, Ho^{3+}), which acts as activator.

* Address correspondence to sailing@kth.se.

Received for review January 11, 2011 and accepted April 22, 2011.

Published online April 22, 2011
10.1021/nn200110j

Mainly through the energy transfer upconversion (ETU) process Yb^{3+} can sequentially absorb two or more photons to efficiently populate the metastable level of activator ion emitting anti-Stokes-shifted lights.[18] This technique offers extremely low autofluorescence background, large anti-Stokes shifts, sharp emission bandwidths, high resistance to photobleaching, nonblinking emission, deep detection ability, and a high spatiotemporal resolution.[18] Recently UCNPs have been attracting remarkable attention in the context of biophotonics areas such as *in vitro* cancer cell imaging,[19−21] *in vivo* tumor targeting imaging,[22,23] multimodal animal imaging,[24−26] high-sensitive biosensing,[27,28] photodynamic therapy,[29,30] and fluorescence diffusing optical tomography.[31,32] UCNPs can emit multicolor light ranging from blue to NIR band by only using a single cost-effective NIR CW laser as excitation. It is quite facile to set up upconversion photoluminescence microscopy by slightly modifying a traditional fluorescence microscope.

To date, NIR laser at a wavelength of about 980 nm is always used to excite UCNPs for upconversion emission in bioimaging due to the fact that the sensitizer ion Yb^{3+} has a high absorption cross-section in its absorption band. However, it is worth pointing out that light around 980 nm suffers from an intrinsic disadvantage: water, as the most significant component of the animal and human body, has a huge absorption peak around 980 nm.[33] Actually, due to this strong water absorption, 980 nm has long been used as a heating optical source in laser thermal therapy before the advent of UCNPs in bioapplications.[34] In the tissue welding fields, the 980 nm laser has also been utilized as a highly effective irradiation light for skin welding.[35] Furthermore, many laser-induced clinical lipolyses have been successfully completed *via* a 980 nm laser effectively heating fat tissue.[36] Therefore, there are two main disadvantages of the 980 nm laser in bioimaging: first, the energy of excitation light would be overwhelmingly attenuated while diffusing in the biological samples. This limited penetration depth will seriously affect the bioimaging efficiency and application extension. Furthermore, almost all the light energy absorbed by biological samples would transform into local heating energy, which could probably induce a considerable elevation of temperature. Indeed, in the context of bioimaging overheating is an undesired side-effect that can affect cell viability and induce tissue damage. This problem is relatively prominent when using 980 nm laser light as an excitation source in many cases and should be avoided when developing these types of autofluorescence-free UC imaging techniques. However, almost all efforts in this development have so far been focused on UCNP synthesis, surface functionalization, and cancer cell or tumor targeting. To the best of our knowledge, there is no reported work with the aim of investigating the tissue overheating effect and penetration depth of 980 nm excitation light while conducting bioimaging. Further optimization in the excitation mode is really needed. Successful translations of the use of autofluorescence-free UC bioimaging from laboratories to clinics require further studies involving the exploitation of larger detection depth and the prevention of overheating irradiation for *in vivo* biomedical applications.

In this paper, for the first time we investigate the overheating effect induced by a 980 nm laser in UCNP-based bioimaging with computational and experimental results. We propose replacing 980 nm laser excitation with 915 nm laser excitation to overcome the most of the overheating issues and to gain improved deep tissue imaging ability. Emission-enhanced monodisperse $NaYbF_4$: Yb^{3+}/Er^{3+}, Yb^{3+}/Ho^{3+}, and Yb^{3+}/Tm^{3+} nanoparticles were prepared according to a modified co-thermolysis method. Then these prepared oleic acid (OA)-capped nanoparticles were further surface functionalized to become hydrophilic, biocompatible, stable, and biotargeting. Before *in vitro* cell imaging, UCNP samples were incubated with the HeLa cancer cell line after conjugated with specific antibody. For *in vivo* mouse imaging these UCNPs were encapsulated with DSPE-mPEG-5000 molecules to render them hydrophilic, stable, and biocompatible in the mouse body. After detailed and reasonable comparison with 980 nm laser light it can be concluded that a larger imaging depth range and biocompatible irradiation were realized in UC bioimaging using a new efficient 915 nm laser excitation method.

RESULTS AND DISCUSSIONS

Optical Absorption Spectra of Water and UCNPs. It is very interesting to find that water, which is completely transparent to the naked eye, has a strong optical absorption in the NIR range (from 930 to 1030 nm), as partly shown in Figure 1a. This plotted curve was duplicated from the original work by Kou *et al.*[33] In this optical wavelength range water has a high absorption peak around the wavelength of about 980 nm (exactly 974 nm). The optical absorption coefficient of pure water at 980 nm is about 0.485 cm^{-1}, indicating that up to 61% of 980 nm light energy will be absorbed by water after propagating a distance of one centimeter in water according to the Beer−Lambert law. When a beam of light is incident into water from air, most of the light will penetrate into the water and the light intensity will be gradually attenuated due to absorption. Almost all the absorbed energy from the shining light will transform into heat energy, which will heat the water and induce significant local elevation of temperature. With such a large absorption coefficient, 980 nm laser light could serve as a heating source for heating water. Adding the fact that water is the most significant component of the animal and human body (60−70%), light around 980 nm is also capable of easily

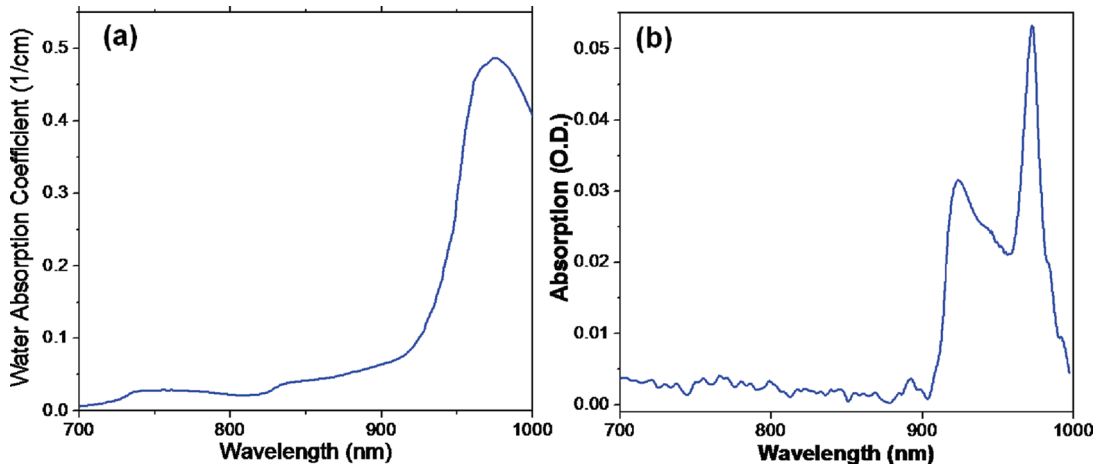

Figure 1. (a) Optical absorption spectrum of water in the NIR range (acquired from ref 33). (b) Absorption spectrum of UCNP colloid suspension.

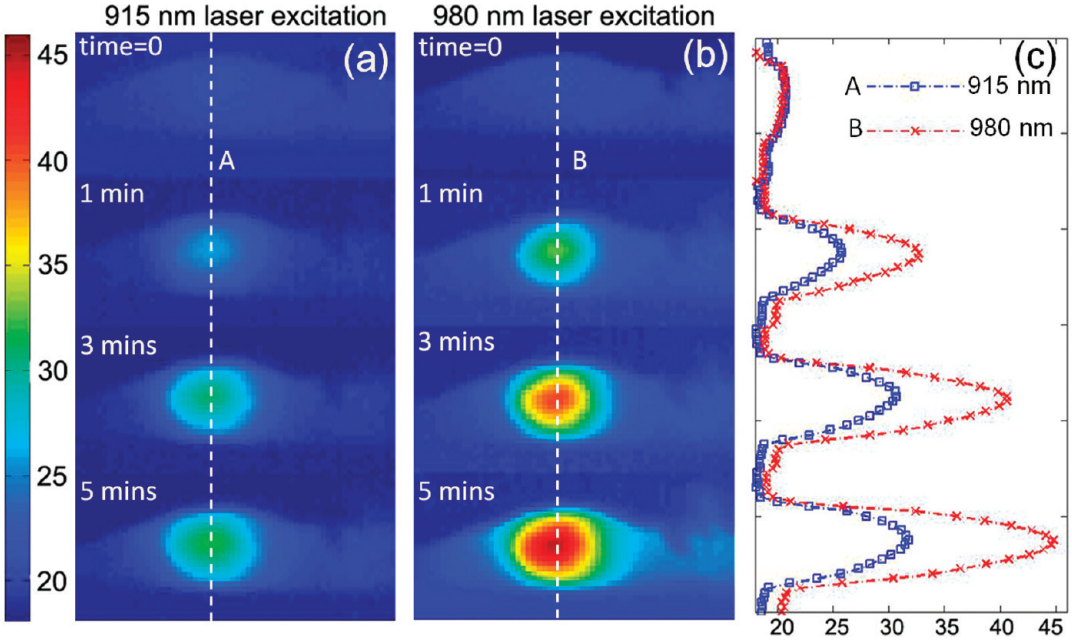

Figure 2. Experimental temperature (°C) distributions after different irradiation times for (a) 915 nm laser irradiated mouse skin and (b) 980 nm laser irradiated mouse skin and (c) the corresponding temperature line profiles (curve A and B in (c) corresponding to line A in (a) and line B in (b), respectively).

heating biological tissue specimens. Nevertheless, 980 nm laser light has been commonly used to excite UCNPs emitting UC photoluminescence in the UC bioimaging modality. In principle, UCNPs can be excited by light from 900 to 1000 nm due to the electron transition absorption between $^2F_{7/2}$ and $^2F_{5/2}$ of Yb^{3+} ions. Excitation with 980 nm laser light may thus not be optimal for their use in bioimaging or biosensing due to potential damage. We used the prepared clear and stable UCNP colloidal suspension (250 mg/mL) to measure the absorption spectrum, and the measured results shown in Figure 1b are similar to the reported results.[37] It can be seen that there is a strong and steep absorption band located in the range 900−1000 nm. Although the maximum absorption occurs around the point of 974 nm, it may still be favorable to utilize light of other wavelengths to excite UCNPs. It is also striking that there is another absorption peak at around 920 nm, where the optical absorption coefficient of water is much lower. For the first time, we propose commercially available 915 nm semiconductor lasers as a new excitation source for UC photoluminescence. The absorption coefficient of water at 915 nm is as low as 0.076 cm^{-1}, less than one-sixth of the value at 980 nm.

Overheating Effect When a 980 nm Laser Is Used. To experimentally investigate and compare the heating effects of a 980 nm laser and a 915 nm laser, two nude mice were exposed to irradiation of the two lasers, and the spatiotemporal temperature distributions were

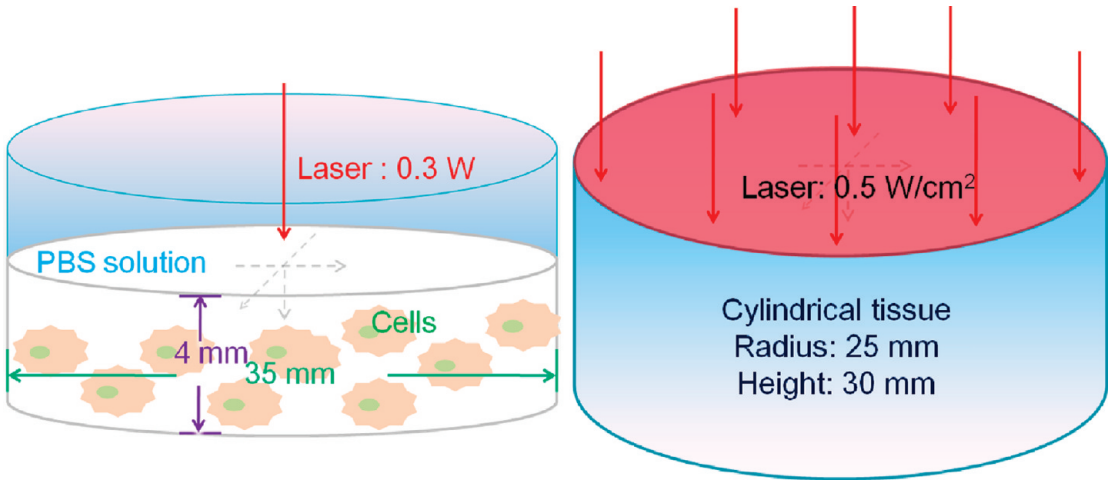

Scheme 1. Schematics of cell-in-celldish (left) and tissue (right) configurations for simulating laser-induced spatiotemporal temperature and photon fluence rate distributions.

monitored. During the UC animal imaging the excitation light has to penetrate through tissues to irritate the UCNPs deeply distributed in the tissue or tumor. To avoid overheating of the tissue, it is important to study the temperature increase induced by the laser irradiation while imaging. In our experiments an anesthetized nude mouse was put on the table with its back exposed to a circular laser beam at a certain incident angle. The laser beams were collimated and expanded to a circular Gaussian beam with a diameter of about 25 mm, and the output power density was tuned to work at the level of 0.5 W/cm^2 (under a stable room temperature of 18 °C). A professional infrared thermal imaging camera was put in front of the mouse to record and analyze the spatiotemporal temperature of the mouse surface. Some temperature images and line profiles are shown in Figure 2. Compared to the pictures in Figure 2a, each picture of Figure 2b has a much higher temperature distribution. Only after one-minute exposure to the 980 nm laser, the temperature in the irradiated area had increased to 33 °C (from an initial temperature of 21 °C). However, in the case of the 915 nm laser this value was as low as 25.8 °C after the same time duration of irradiation. As the irradiation time increases, the difference in temperature rises became larger. After two and three minutes, the 980 nm laser heated the mouse to 41 and 45 °C, respectively, whereas it was only 31.4 and 32.3 °C for the 915 nm exposure. When the process reached its steady state, the 980 nm beam heated the mouse skin to a temperature as high as 49.2 °C. Larger power density would be required for realizing deep *in vivo* imaging. In these cases a 980 nm laser may induce higher temperature elevation. After this experiment the 980 nm laser irradiated area of mouse skin was seriously damaged, and an evident scar appeared (picture not shown). [Note that high temperatures (above 50 °C) are used for ablation (direct destruction) of some tumors or other tissues clinically.] This did not happen to the other mouse exposed to the 915 nm laser. From the above comprehensive comparisons, we can easily conclude that a remarkable overheating effect could be induced in a mouse *in vivo* imaging by 980 nm laser irradiation. An alternative 915 nm laser can effectively overcome this serious problem.

Comparison of 915 nm Laser and 980 nm Laser Induced Temperature Elevations in Cell Imaging. A 980 nm laser could easily heat the PBS solution, which may produce cell damage and even cell death in cell imaging.[38−40] To rigorously demonstrate that 915 nm laser light can avoid an overheating effect during *in vitro* cell imaging, we designed a cell-in-celldish model with systematical and reasonable parameter settings (*e.g.*, excitation power: 300 mW) consistent with practical imaging conditions, as shown in Scheme 1. In the microscopy the excitation light has to go through a layer of liquid (*e.g.*, cell growth solution or PBS solution). In this case the energy lost from both the exciting and emitting lights while penetrating the PBS buffer solution should be taken into consideration since the exciting light or emitting light would likely be absorbed by this liquid layer. In the UC bioimaging, the exciting light (980 nm) is absorbed significantly by water. Herein, we computationally investigated the lost laser energy and the laser-induced temperature elevation outcome. The cells are adhered to the bottom of a 35 mm celldish filled with 2 mL of PBS (live cell environments: 5% CO_2, 37 °C). It was found that the accumulated temperature elevation depends on the laser irradiation time. [Even though the focal/scanning dot is moving during the confocal imaging, and the scanning area is quite small compared to the whole cell dish. The accumulated thermal effect is nearly the same as the case of irradiation at one fixed dot. We assume the laser incident point is fixed in the simulation.] After 30 s of irradiation, the temperature rises induced by these two lasers were not significant, as shown in Figure 3a,b. In spite of a temperature difference of about 0.7 °C, the whole

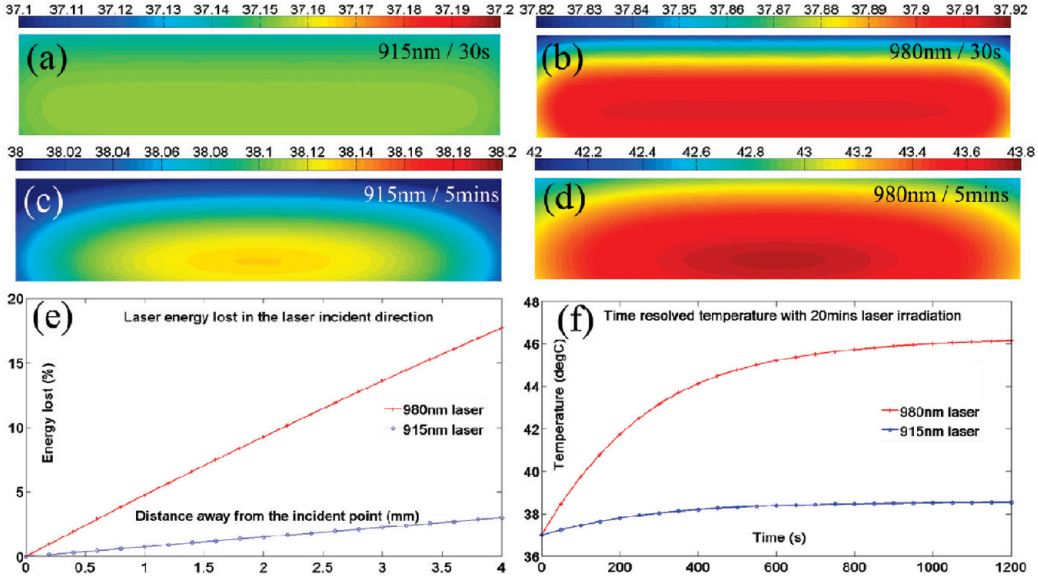

Figure 3. Simulated results of cell-in-celldish imaging model: excitation laser induced temperature (°C) distributions after (a, b) 30 s and (c, d) 5 min of irradiation with (a, c) a 915 nm laser and (b, d) a 980 nm laser; (e) percentages of the lost laser energy while penetrating through the PBS solution; (f) time-resolved temperature at the point (0, 0, 0.5 mm) where the adhered cells are located during 20 min irradiation.

temperature was below 38 °C. It is indicated that in some simple and quick imaging processes (*e.g.*, 2-D intensity imaging) the laser heating effect could be negligible. Other than the simplest 2-D imaging, some 3-D imaging and 4-D imaging are also commonly used and needed in many studies. In these cases, the continuum irradiation time should be much longer. Several minutes of irradiation (*e.g.*, 5 min or longer) is quite possible in the applications of multidimensional scanning and real-time monitoring (continuum imaging of, for example, cell division, cell fusion, cell death, and nanoparticle behavior inside cells). Parts (c) and (d) of Figure 3, respectively, showed 915 and 980 nm exciting light induced temperature distributions after 5 min of irradiation. These two vertical cross-section maps clearly describe the spatial temperature distributions and their significant difference in temperature elevation. The highest temperature area occurred near the center of the bottom (where the adhered cells are located), and the decreasing trend was observed from inside to outside due to heat transfer process. The picture in Figure 3c indicates that the 915 nm laser heated the solution from 37 °C (initial temperature) to 38.1 °C with only a rise of 1.1 °C. However, as depicted in Figure 3d 980 nm light rendered the temperature in most areas on the order of about 44 °C, which is higher than the hyperthermia treatment temperature for cell apoptosis.[38,39] In this case the 980 nm laser may lead to characteristic cell changes (morphology) and death. [These changes may include bleb, loss of cell membrane asymmetry and attachment, cell shrinkage, nuclear fragmentation, chromatin condensation, and chromosomal DNA fragmentation.] Fortunately, most of the damage to the cells could be avoided by using 915 nm instead of 980 nm light because the temperature was kept at a low (38.1 °C) and apoptosis-free level, as shown in Figure 3c. The red and blue lines plotted in Figure 2f show the time-resolved temperature profiles at the point 0.5 mm above the center of the bottom with 20 min laser irradiation. After 3−4 min excitation the temperature rapidly reached the apoptosis level (42 °C), and longer irradiation could induce a high temperature of about 46 °C. This significant difference between the two curves could easily be attributed to the fact that much more energy from the 980 nm light goes to water heating. As seen in Figure 2e about 18% of the 980 nm laser energy was absorbed by the 4 mm PBS solution layer, while only 3% of the 915 nm energy was absorbed. The data not only confirmed the overheating effect of 980 nm laser but also demonstrated the nonoverheating effect of the 915 nm laser and its potential for *in vitro* UC bioimaging applications of microscopy systems.

Comparison of 915 nm Laser and 980 nm Laser Induced Temperature Elevations in Tissue Imaging. Though many efforts have been made to extend UCNP applications into *in vivo* imaging and phantom diffusing optical imaging very recently,[41−44] the imaging depth was still very low (all below 1 cm, *e.g.*, intravenous injection, under-skin tumor/tissue in little nude mouse and not deep inclusion in phantom). Furthermore, very few theoretical and experimental studies were done to investigate the temperature outcome induced by 980 nm laser light in the imaging process. With the purpose of clinical applications, larger imaging depth and nonoverheating irradiation should be realized. The use of the 915 nm laser can help to overcome the

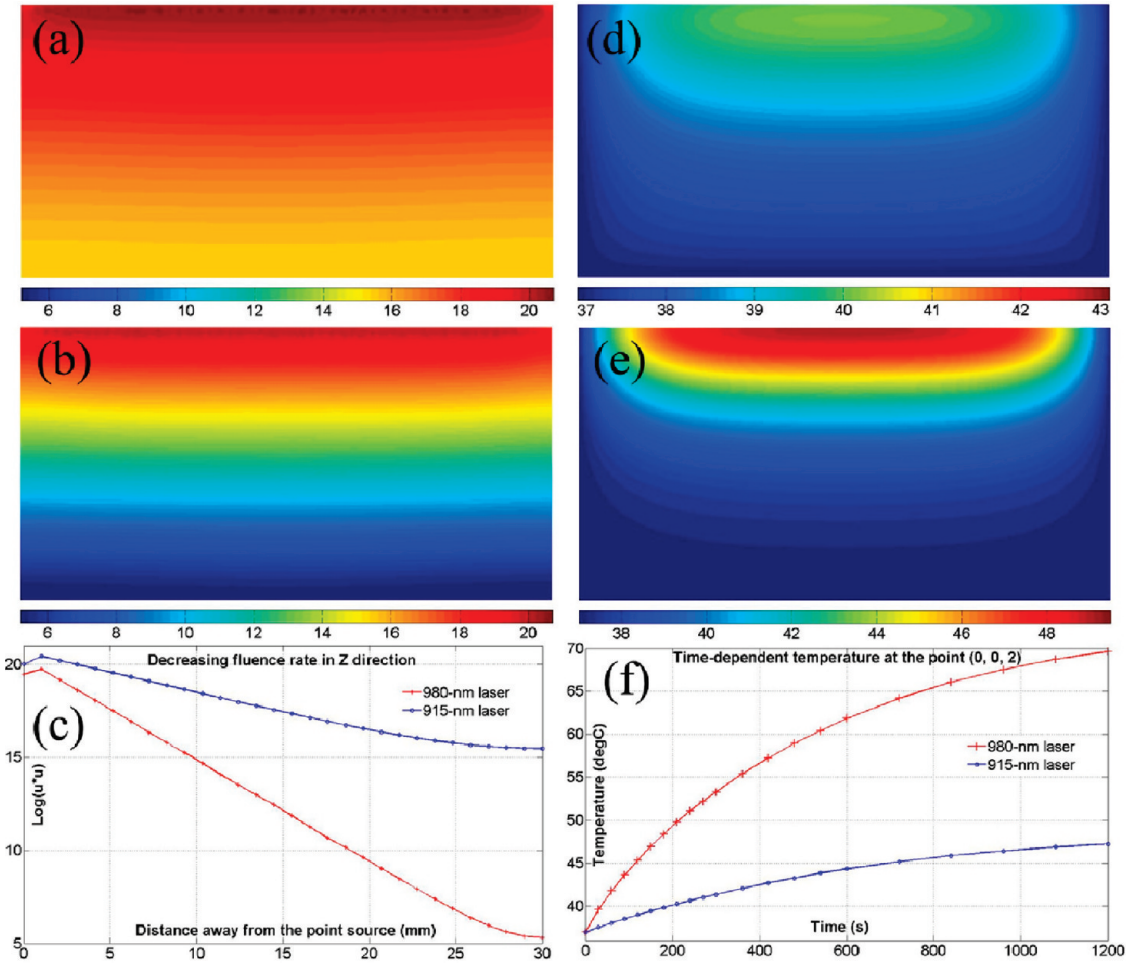

Figure 4. Simulated distributions of temperature and photon fluence rate (u) in the phantom: the logarithm of square excitation photon fluence rate (log(u^2)) of (a) a 915 nm laser and (b) a 980 nm laser; (c) log(u^2) as a function of the imaging depth while the laser transmits light into the phantom; cross-sectional distribution of the laser-induced temperature (°C) after 3 min irradiation of (d) a 915 nm laser and (e) a 980 nm laser; (f) time-resolved temperature at point (0, 0, 2 mm) during 20 min of irradiation.

problem induced by the strong 980 nm light absorption of tissue. To elucidate the advantages of 915 nm laser light in UC imaging, a theoretical model was designed to computationally investigate the temperature outcome and imaging depth in tissue imaging. As shown in Scheme 1, a cylindrical phantom (height 3 cm; radius 2.5 cm) was modeled to simulate a human tissue with typical tissue optical and heat transfer parameters settings.[45,46] [Similar to many other reported works within the field of biomedical optics,[32,47] a tissue phantom with uniform optical properties and thermal properties was also used in our model.] One circular laser beam with a diameter of 50 mm and a typical power density of 0.5 W/cm^2 was set to vertically incident from the center of the top phantom surface. Even though imaging could be realized with low power density and short irradiation time if one uses an EMCCD (extremely expensive and highly sensitive, designed to detect single photons),[19,24,43] this power density (0.5 W/cm^2 or a bit higher) is quite desirable in the case of deep tissue imaging or when only a cost-effective common CCD is available (like in the present work). The diffusion equation was used to model the propagation of the excitation light photon in the turbid phantom.[48] The photon fluence rate (u) refers to the total number of photons incident from all directions on a small sphere divided by the cross-sectional area of the sphere and per time interval (SI unit: m^{-2} s^{-1}). Then the absorbed photon energy was transformed into heat energy, which was modeled using the classical heat transfer equation. Due to the much larger absorption coefficient, 980 nm light could be rapidly absorbed by tissue phantom, while the 915 nm laser light could penetrate through a deeper distance, as shown in Figure 4a–c. Compared to Figure 4a, the square of the photon fluence rate (u^2) in Figure 4b has a more concentrated distribution near the incident area. Low absorption enables the 915 nm photon to extend to a more dispersive distribution. The two curves in Figure 4c indicate that along the incident direction the 915 nm light has an about 40 times larger u^2 value than the 980 nm light after 1 cm transport. As the

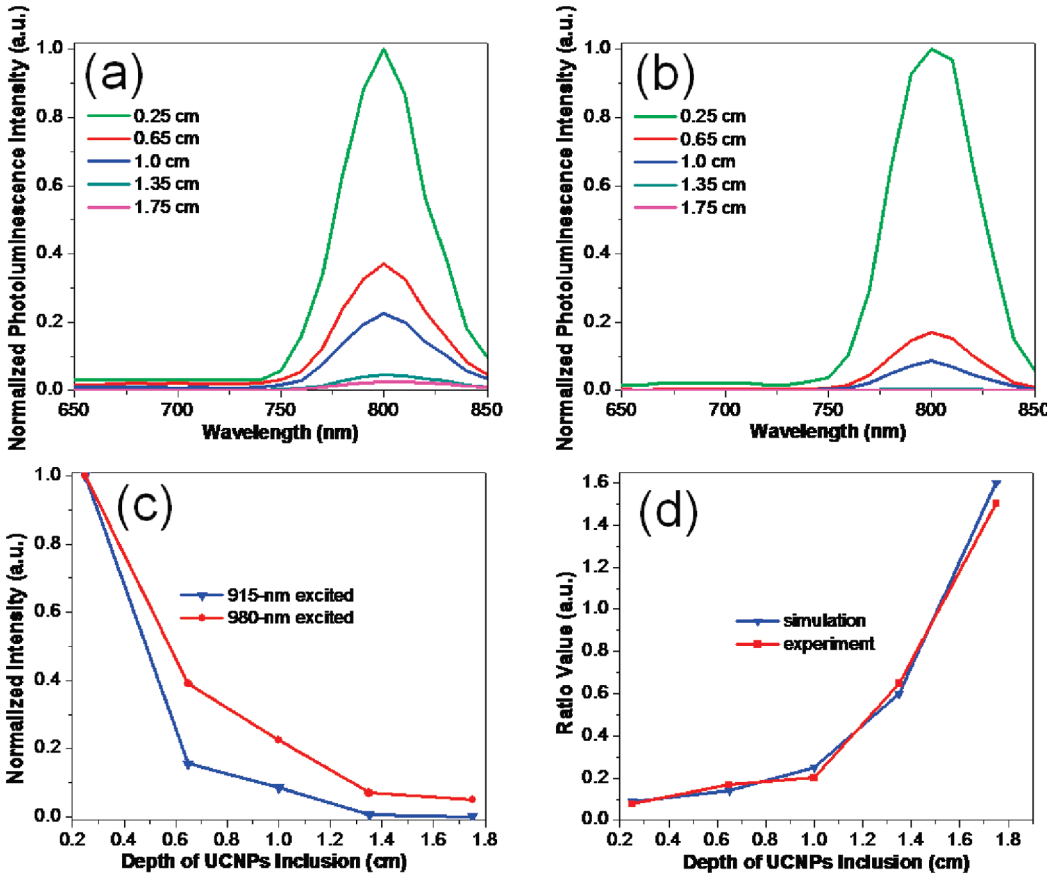

Figure 5. Decreasing intensity (detected on the phantom surface) of UC photoluminescence from $NaYbF_4$: Yb^{3+}/Tm^{3+} inclusion embedded in the phantom with increasing depth (0.25, 0.65, 1, 1.35, 1.65 cm) excited by (a) a 915 nm laser beam and (b) a 980 nm laser beam; (c) the intensity of the UC signal at fixed excitation illumination as a function of the depth of the UCNP inclusion and (d) the peak intensity ratios (for both the experimental and simulated data) of UC photoluminescence intensities (detected on the surface) for each depth for 915 nm excitation and 980 nm excitation.

imaging depth increases, the 980 nm light will vanish much more rapidly than the 915 nm light, indicating that 915 nm is more capable for deeper imaging. The lost energy of the laser light became the thermal energy and heated the whole phantom with the temperature profiles shown in Figure 4d–f. The phantom was set to an initial temperature of 36.5 °C (human body temperature), and after 3 min of 915 nm laser irradiation, the highest temperature of 40.2 °C was reached near the incident area (a certain volume around 39 °C). On the contrary, having much more light energy transferring to heat energy, the 980 nm laser heated the phantom to a temperature up to 49.6 °C with a big volume above 45 °C. According to the time-resolved profiles shown in Figure 4f, the difference in temperature rises gets larger as the irradiation time increases. This big difference can easily be attributed to the fact that a 980 nm laser acts as a more effective optical heating source.

Comparison of the Deep Tissue Imaging Abilities of 915 nm Laser and 980 nm Laser. The upconversion photoluminescence process is a two-photon nonlinear effect (three-photon for blue emission). Compared to the linear emission process of traditional dyes, this nonlinear effect of UCNPs gives UC luminescence a quicker descent trend with increasing imaging depth (quadratic power dependence).[49] Thus, to suppress this disadvantageous effect, an excitation light with low tissue absorption is required for realizing deep imaging. We did some phantom experiments to further demonstrate the advantage of the 915 nm laser for deep UC imaging. In our experiments, the imaging setup is similar to our previously reported work.[50] We prepared an optically tissue-equivalent phantom that consists of intralipid and black India ink with typical human tissue optical properties. A small glass tube filled with as-synthesized $NaYbF_4$: Yb^{3+}/Tm^{3+} nanoparticle chloroform suspension as photoluminescence inclusion was embedded in the phantom solution at five different depths (0.25, 0.65, 1, 1.35, and 1.75 cm). The well-prepared samples were imaged with a Maestro imaging system (CRI, Inc., Woburn, MA) equipped with 915 and 980 nm lasers (2 W/cm^2). At each depth the UC photoluminescence image was captured by CCD, and at the same time the spectral information was recorded using the tunable liquid crystal filters. With the increasing depth of UCNP inclusion, the signal intensity decreased because a

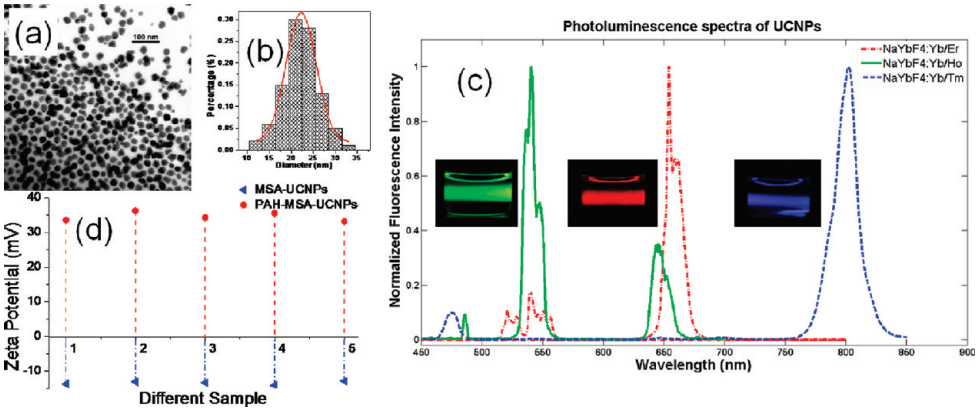

Figure 6. TEM images of (a) synthesized $NaYbF_4$: Yb^{3+}/Er^{3+}; (b) diameter distribution of UCNPs in (a). (c) Photoluminescence spectra of $NaYbF_4$: Yb^{3+}/Er^{3+} (red emission), $NaYbF_4$: Yb^{3+}/Ho^{3+} (green emission), and $NaYbF_4$: Yb^{3+}/Tm^{3+} (blue emission). The insets show the visible photoluminescence imaging of the UCNP colloidal suspension excited by a 915 nm laser (500 mW/cm^2). (d) Zeta potential measurements of five different MSA-UCNP and PAH-MSA-UCNP samples.

deeper position requires that both the excitation and emission lights have to experience much more scattering and absorption. The five curves in Figure 5a,b show the spectra and normalized intensity of UC photoluminescence excited by 915 and 980 nm lasers, respectively. The peaks at 800 nm wavelength verified that the photoluminescence was truly emitted from $NaYbF_4$: Yb^{3+}/Tm^{3+}. After comparison one can easily see that the five peak intensities in Figure 5b have a more rapid descent trend than those in Figure 5a, which is shown in Figure 5c. This could be attributed to much higher water absorption at 980 nm wavelength. Due to the nonlinear emission process, UCPN-based tissue imaging has a more rapid descent trend than traditional linear dyes as the imaging depth increases.[49] Therefore, the tissue absorption should be small at the excitation wavelength in order to overcome this problem. The experimental and simulation UC signal intensity ratio (915 nm excited emission over 980 nm excited emission) was plotted as a function of inclusion depth in Figure 5d. Since 980 nm light has a higher excitation efficiency, the ratio value is low in the small depth range (about 0.08 at a depth of 0.25 cm). When the depth becomes larger, this ratio value increases sharply as 980 nm light intensity decreases significantly. At a depth of 1.75 cm a ratio value of 1.53 was achieved, which means 915 nm light excited 50% more intense UC photoluminescence than 980 nm light did. Simulations based on a fluorescence diffusion imaging model (diffusion equations for both the excitation light and the emission light) were performed to compare with the experimental results.[41] As shown in Figure 5d, the simulated peak intensity ratio at each depth and the overall trend agree well with the experimental data. When we increased the imaging depth to 1.85 cm, a 980 nm laser could not excite high enough UC signals for detection on the surface, but a 915 nm laser still could. It is reasonable to assume that there is a minimal power density for excitation at a specific depth so that the UC signal can be detected on the surface. In practice the required minimal excitation power density depends on many factors such as the sensitivity of the photon detector, the amount and concentration of excited UCPNs, and the optical properties of the tissue. Thus the threshold is a comprehensive issue and would strongly depend on the experimental conditions. By combining the experiments and calculations, we tried to find the photon fluence rate threshold under our present experimental conditions (*e.g.*, without expensive EMCCD). For example, according to our experimental results, to excite UCNPs at a depth of 1.85 cm, a 980 nm light excitation would require a minimal power density of 2 W/cm^2, which would easily induce an apparent overheating effect. However, with 915 nm light excitation, only 1.5 W/cm^2 is sufficient to excite UCNPs at this depth. We have shown both experimentally and computationally that 915 nm laser excitation is advantageous for deep tissue imaging compared to 980 nm laser excitation.

Preparation and Characterization of UCNPs. In our experiments the UCNPs were synthesized according to the method previously reported, with some modifications.[51,52] To obtain the UC photoluminescence intensity enhanced UCNPs, we chose to prepare Yb-enhanced $NaYF_4$ material for UCNPs.[37] Three different rare earth ions, doped with $NaYbF_4$: Yb^{3+}/Er^{3+}, Yb^{3+}/Ho^{3+}, and Yb^{3+}/Tm^{3+}, were synthesized separately, to emit light with different colors (red, green, and blue, respectively, as shown in the inset pictures in Figure 6c). These as-prepared UCNPs could form a clear, transparent colloidal suspension in both chloroform and cyclohexane. The size and shape of the UCNPs were characterized by transmission electron microscopy (TEM). The representative TEM image in Figure 6a shows that these are well-dispersed $NaYbF_4$: Yb^{3+} /Er^{3+} with a mean diameter of about 22 nm and a relatively narrow size distribution, as shown in Figure 6b, indicating favorable

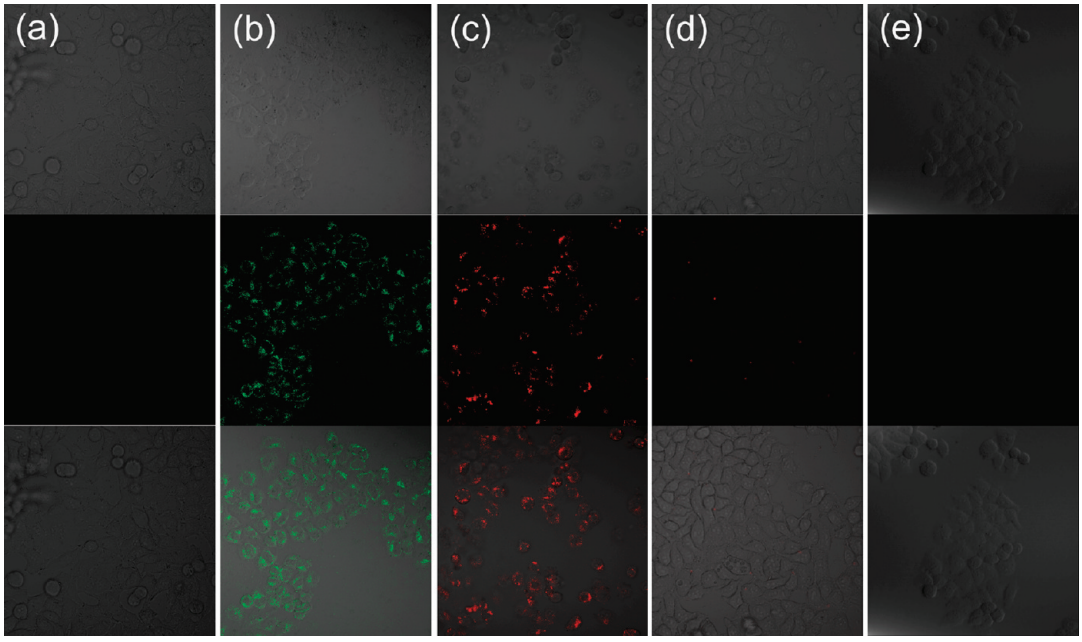

Figure 7. ***In vitro*** **cancer cell imaging using 915 nm laser excited UCNPs: images of HeLa cells separately incubated with (a) nothing as blank, (b) anti-CEA8-PAH-MSA-NaYbF$_4$: Yb^{3+}/Ho^{3+}, (c) anti-CEA8-PAH-MSA-NaYbF$_4$: Yb^{3+}/Er^{3+}, (d) PAH-MSA-NaYbF$_4$: Yb^{3+}/Er^{3+}, and (e) anti-CEA8-PAH-MSA-NaYbF$_4$: Yb^{3+}/Er^{3+} in the presence of a 10-fold excess of unlabeled anti-CEA8. Bright field images (upper row), photoluminescence images (middle row), and superimposed images (bottom row).**

nanoparticle morphology for bioimaging and biosensing (TEM images and size distributions of NaYbF$_4$: Yb^{3+}/Ho^{3+} and Yb^{3+}/Tm^{3+} are shown in Figure S1). Phase compositions of NaYbF$_4$: Yb^{3+}/Er^{3+} were determined by X-ray powder diffraction, and the patterns (Figure S2) indicate the face-centered cubic structure of the prepared UCNPs. For the purpose of bioapplications, the as-synthesized OA-capped UCNPs were first rendered aqueous dispersible through 5-mercaptosuccinic acid (MSA) encapsulation. Then negatively charged MSA-UCNPs were further polymer-coated through physical adsorption by polyallylamine hydrochloride (PAH), which is a kind of polymer with a strong positive charge. Zeta potential test (Figure 6d) showed MSA-UCNPs and PAH-MSA-UCNPs were negatively charged and positively charged, respectively. The significant decrease of OA, MSA encapsulation and PAH coating was also confirmed by Fourier transform infrared spectroscopy (FTIR) (Figure S3). PAH was introduced to encapsulate UCNPs, as it can play three significant roles here. First, the positively charged surface of the nanoparticle is desired and allows antibody protein molecule conjugation. The antibody chosen here is anti-CEA8, which has a pI value within 5.8−6.5 (data from Supply Corporation). In the PBS solution environments (pH 7.4) anti-CEA8 carries a negative charge and can be conjugated with PAH-MSA-UCNPs through noncovalent bonding. Second, the cytotoxicity of nanoparticles used for cell imaging is an important issue and should be avoided. PAH polymer coating has been reported as an effective and biocompatible encapsulation for various nanoparticles. In the experiments, PAH-MSA-UCNPs showed hardly any toxicity to the cell lines. Third, with strong positive charge on their surfaces UCNPs would repel one another to form a stable solution without aggregation. The PAH-MSA-UCNPs were further conjugated with the antibody anti-CEA8 through noncovalent bonding in PBS.[53] The prepared PAH-MSA-UCNP aqueous colloidal suspensions were used in spectroscopy measurements to determine their UC photoluminescence spectra (excited at 915 nm). The emission bands and inset pictures in Figure 6c indicated that radiative deactivation of the upconverted 915 nm light energy occurs through visible or NIR emission. These also show the 915 nm laser excitation efficiency of the UC photoluminescence and their great potential in optical bioimaging.

Targeting HeLa Cancer Cells Imaging Using 915 nm Laser Excited UCNPs. To determine whether 915 nm laser excited UCNPs can be used as potential optical tags for cellular studies, we performed *in vitro* HeLa and MDA cancer cell imaging using a confocal microscopy system equipped with a 915 nm semiconductor laser (300 mW). PAH-NaYbF$_4$: Yb^{3+}/Ho^{3+} with green emission and PAH-NaYbF$_4$: Yb^{3+}/Er^{3+} with red emission were chosen as optical probes, and they were immunolabeled with rabbit anti-CEA8 antibodies, which is commonly used to immunologically detect the carcinoembryonic antigen (CEA), a cancer biomarker expressed on the surface of HeLa cells.[20] The well-prepared anti-CEA8-conjugated UCNPs were incubated with HeLa cancer cell lines for two hours before confocal scanning. Figure 7 shows the UC photoluminescence images of HeLa cancer cell lines after different treatments. The cells in picture (b) were remarkably stained

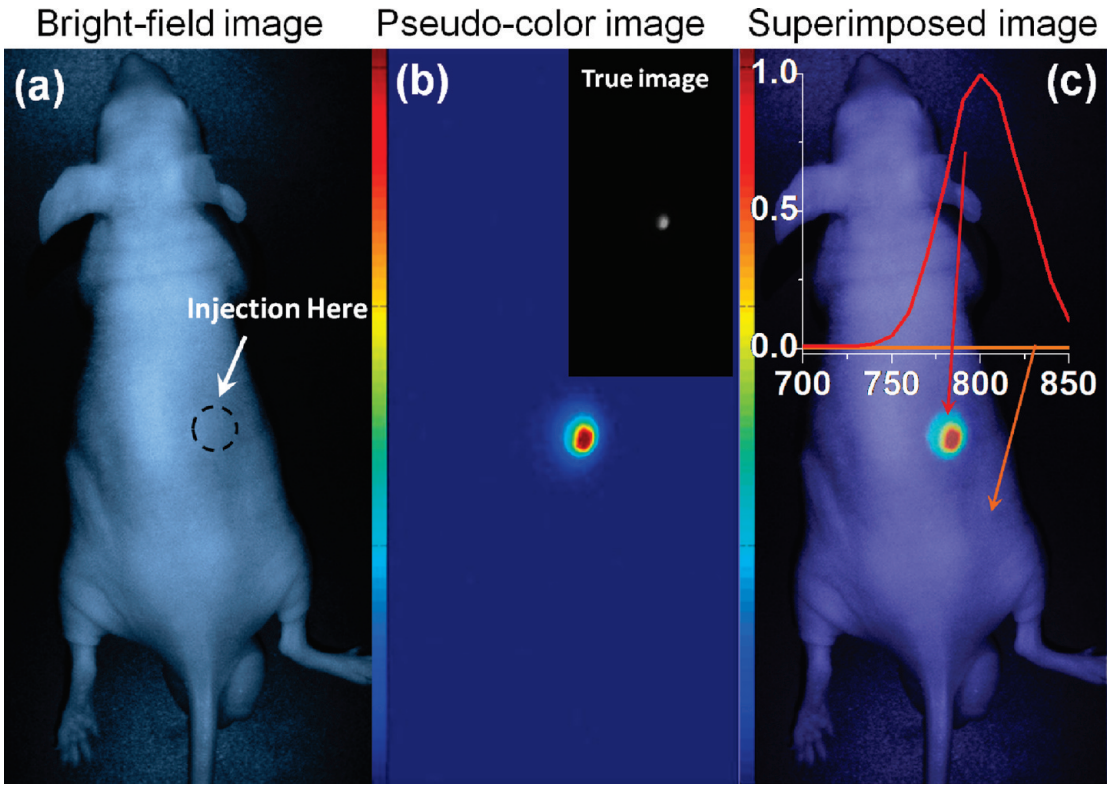

Figure 8. *In vivo* **whole body image of a $NaYbF_4$: Yb^{3+}/Tm^{3+} injected nude mouse: (a) bright field image, (b) pseudocolor image obtained from true image (the inset black/white image), and (c) superimposed image (bright field image and pseudocolor image) with the unmixed spectra of *in vivo* image (the inset chart) of UC signal and background as indicated by the arrows.**

with strong bright green emission from $NaYbF_4$: Yb^{3+}/Ho^{3+}, which indicates that HeLa cells have taken up anti-CEA8-PAH-MSA-$NaYbF_4$: Yb^{3+}/Ho^{3+} through the specific immunolabeling recognition. Superimposing the bright field image and UC photoluminescence image, we can easily find that all the green emission was from the cell surface (little emission elsewhere). Similar to other reported works,[19,21] two control experiments were carried out in order to further confirm the specific nature of antibody-mediated targeting on cancer cells. In picture (d), the cells incubated with PAH-MSA-$NaYbF_4$: Yb^{3+}/Er^{3+} were rarely stained by red emission because of a very low possibility of labeling most cells. The specific immunolabeling recognition of anti-CEA8-PAH-MSA-UCNPs was further demonstrated by a competition experiment. The HeLa cells were preincubated with a 10-fold excess of unlabeled anti-CEA8 for about half an hour and then incubated with anti-CEA8-PAH-MSA-UCNPs for another half hour. As shown in Figure 7e nearly no red emission could be observed, indicating very few UCNPs were taken up by cells. These facts confirmed the UC photoluminescence excited by the 915 nm laser was strong enough for the cell imaging and the successful specific targeting ability of the anti-CEA8-PAH-MSA-UCNPs into the HeLa cancer cells. Figure 7a shows the imaging pictures of blank cell lines (with UCNPs), and no emission could be observed in the completely dark fluorescence image (middle row), indicating that no autofluorescence from cells themselves was excited by the 915 nm laser. All the above experimental results demonstrate that 915 nm laser light could be used to efficiently excite UCNPs attached on HeLa cancer cells for autofluorescence-free optical bioimaging.

***In Vivo* Nude Mouse Imaging Using 915 nm Laser Excited UCNPs.** To demonstrate the ability of 915 nm laser excitation for *in vivo* UC bioimaging, $NaYbF_4$: Yb^{3+}/Tm^{3+} nanoparticles were injected into the skin of a nude mouse. The subcutaneously injected mouse was immediately imaged with a Maestro *in vivo* imaging system equipped with a 915 nm laser (1.25 W/cm^2). We chose $NaYbF_4$: Yb^{3+}/Tm^{3+} nanoparticles as optical tags because their strong NIR (800 nm) UC photoluminescence has a quite low absorption of animal or human tissue, facilitating large imaging depth. DSPE-mPEG-5000 was employed to directly encapsulate OA-capped $NaYbF_4$: Yb^{3+}/Tm^{3+} to make nanoparticles hydrophilic and biocompatible and prevent aggregations in biological environments. Figure 8 shows the whole body *in vivo* image of a nude mouse injected with DSPE-mPEG-5000-UCNPs with (a) bright field image, (b) pseudocolor UC photoluminescence image, and (c) their superimposed image. A quite

high-contrast emission picture was observed in the experiments (Figure 8b). After overlaying the bright field and pseudocolor image, we found that the bright emission occurred where the DSPE-mPEG-5000-UCNPs were injected, and almost no autofluorescence was observed elsewhere. Unmixed spectrum analysis with a wavelength range from 700 to 850 nm (the curves in Figure 8c) also testifies that 915 nm laser light greatly excites DSPE-mPEG-5000-UCNPs to emit 800 nm UC photoluminescence. The strong and sharp emission band around 800 nm corresponds to the treated skin area, as the red arrow indicates, while the flat line corresponds to the untreated areas, as the orange arrow indicates. This *in vivo* animal imaging experiment successfully demonstrated the great potential of 915 nm laser excitation for autofluorescence-free UCNPs-based UC animal imaging.

CONCLUSIONS

In this paper, we have experimentally and computationally studied the overheating effect of 980 nm laser irradiation in the UC optical bioimaging. A new efficient excitation approach using 915 nm laser light was proposed for the first time to excite UCNPs to emit UC photoluminescence for bioimaging. Compared with 980 nm laser light, 915 nm laser light has much lower water absorption and induced a much lower temperature rise, acceptable to animal skin. Our phantom imaging experiments have demonstrated that the 915 nm laser excitation method can achieve larger imaging depth range in tissue and animal imaging. Emission-enhanced monodisperse $NaYbF_4$: Yb^{3+}/Er^{3+}, Yb^{3+}/Ho^{3+}, and Yb^{3+}/Tm^{3+} nanoparticles have been synthesized and characterized. Antibody anti-CEA8 conjugated PAH-MSA-UCNPs and DSPE-mPEG-5000-UCNPs were synthesized using facile methods and subsequently used for *in vitro* and *in vivo* bioimaging studies, respectively. The 915 nm laser excited UCNPs have been used for HeLa cancer cell imaging and nude mouse *in vivo* imaging, and good experimental outcomes have been achieved. Overall, the efficiency and advantages of the 915 nm laser excitation approach have been successfully verified. The proposed method enables one to further develop deeper tissue/tumor UC bioimaging with biocompatible laser irradiation.

METHODS

Theoretical Model. As shown in Scheme 1, the configurations and dimensions for simulation are given in detail. Simulations were employed for both *in vitro* cell imaging and *in vivo* imaging based on the photon diffusing equation and the heat transfer conduction equation to study 980 nm laser and 915 nm laser induced spatiotemporal temperature and photon fluence rate distributions.

Cell-in-Celldish Model: The temperature distribution model for *in vitro* cell-in-celldish is based on the transient heat transfer equation with an additional term to account for energy absorbed by PBS.

$$\rho c(\partial T/\partial t) = \nabla(k\nabla T) + Q$$

where T(K) is the solution temperature, t(s) is time, $\rho = 10^3$ (kg/m^3) the density of the PBS solution, $c = 4200$(J/kg·K) is the heat capacity of the PBS solution, $k = 0.58$(W/m·K) is the thermal conductivity of the PBS solution ,Q(W/m^3) is the heat source. ($Q_{980\ nm} = 130\,270$, $Q_{915\ nm} = 22000$, according to Lambert−Beer law.) The ratio $k/\rho c$ is called the thermal diffusivity (m^2 s^{-1}), which describes the dynamic behavior of the thermal process. Regarding the boundary conditions used to solve the heat transfer model, a heat flux or Neumann boundary condition was used in conjunction with Newton's law of cooling to give

$$k(\partial T/\partial n)) = h(T - T_0)$$

where h is the overall heat transfer coefficient for the region adjacent to the model boundary, and T_0 (37 °C) is the bulk temperature of the surroundings. Typical values of h_{air} = 25-(W/(m^2·K)), h_{wall} = 5(W/(m^2·K)) were used in the model.

Tissue Model: The diffusion equation was used to model the propagation of the excitation light photon in the turbid phantom.[48] The photon fluence rate refers to the total number of photons incident from all directions on a small sphere divided by the cross-sectional area of the sphere and per time interval. Then the absorbed energy was transformed into heat energy, which was modeled using the transient heat transfer equation. We used the Helmholtz representation of the diffusion equation in the steady state:

$$\nabla(-D\nabla\varphi) + \mu_a\varphi = S,\ D = 1/(3(\mu_a + \mu_s'))$$
$$\rho c(\partial T/\partial t) = \nabla(k\nabla T) + Q,\ Q = \mu_a\varphi$$

where φ(m^{-2} s^{-1})is the photon fluence rate represented, D is the diffusion coefficient, μ_a(m^{-1}) is the absorption coefficient of the tissue, μ_s'(m^{-1}) is the reduced scattering coefficient of the tissue, S represents the source term, and the absorbed photon fluence rate $\mu_a\varphi$ was the heat source term. One commonly used boundary condition that accounts for the refractive index mismatch between tissue ($n \sim 1.4$) and air ($n \sim 1$) is the Robin-type boundary condition.[54]

$$\varphi + 2AD(\nabla\varphi)\vec{n} = 0$$

Calculation of A for a tissue−air interface with $n_{tissue} = 1.4$ and $n_{air} = 1$ yields $A = 2.74$. The boundaries other than the top surface of the refractive index mismatch are continuous boundary conditions (the tissue of interest was regarded as a part of one whole human body). Term D is the diffusion coefficient. The absorption coefficient and reduced scattering coefficient were set as typical values according to ref 45 and absorption spectra of biological specimen.[55]

Materials. Lanthanide oxides (Tm_2O_3, Yb_2O_3, Ho_2O_3, and Er_2O_3), trifluoroacetic acid (99%), sodium trifluoroacetate (98%), 5-mercaptosuccinic acid, and polyallylamine hydrochloride were purchased from Sigma-Aldrich. All lanthanide oxides utilized were 99.99% purity or higher. Octadecene (90%), oleic acid (90%), anhydrous ethanol, anhydrous methanol, ammonia aqueous (~30%), cyclohexane, and chloroform were purchased from Sinopharm Chemical Reagent Co. (China). The antibody anti-CEA8 (anti-CEAcam8/CD67) was purchased from Beijing Biosynthesis Biotechnology Co., Ltd. DSPE-mPEG-5000 (1,2-distearoyl-*sn*-glycero-3-phosphoethanolamine-*N*-methoxy (polyethylene glycol)-5000) was purchased from Creative PEGWorks, Inc. Intralipid was purchased from Zhejiang University Hospital. All of the chemicals were used without further purification, and

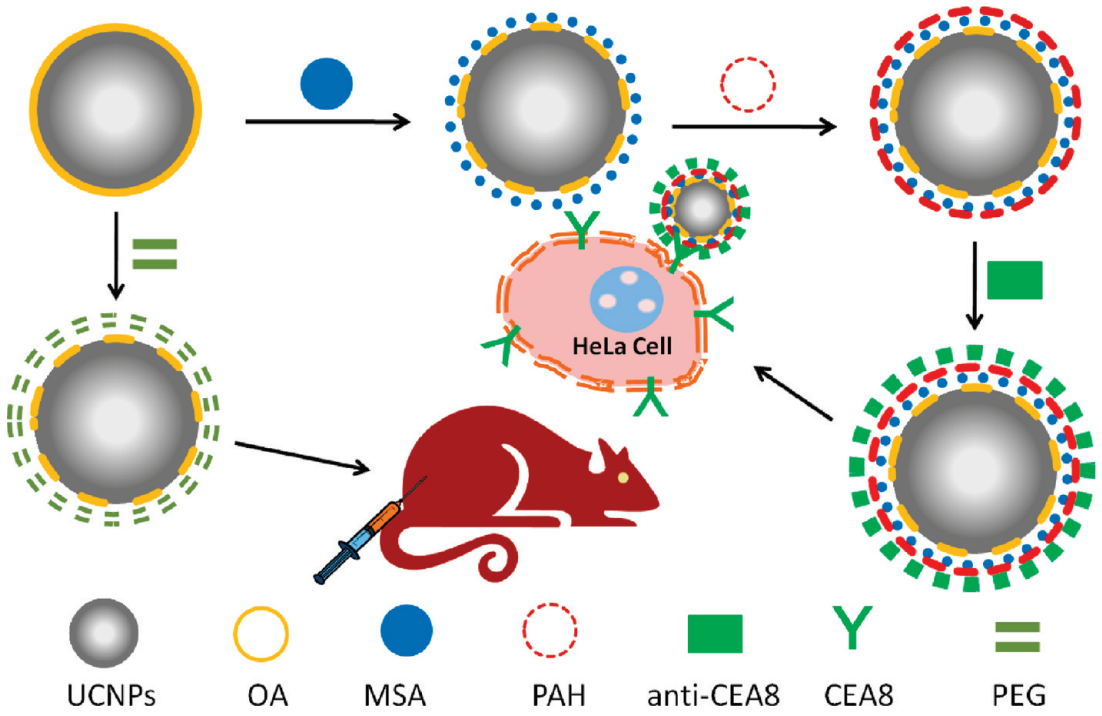

Scheme 2. Schematic diagram illustrating the hydrophilization and coating of hydrophobic OA-capped UCNPs, the bioconjugation between PAH-MSA-UCNPs and antibody anti-CEA8, and the incubation of antibody-conjugated anti-CEA8-UCNPs with HeLa cancer cells. DSPE-mPEG-5000-UCNPs were intravenously injected into a nude mouse for *in vivo* animal imaging.

deionized (DI) water was used in the experimental procedures. HeLa cancer cell lines were supplied by the Medical School of Zhejiang University. The studied mice (18−21 g weight male nude mice) were purchased from Animal Experimentation Center of Zhejiang University).

Synthesis of $NaYbF_4$: Yb^{3+}/Er^{3+}, Yb^{3+}/Ho^{3+}, and Yb^{3+}/Tm^{3+} Nanoparticles. The $NaYbF_4$: Yb^{3+}/Tm^{3+} (98 mol % Yb^{3+} and 2 mol % Tm^{3+}, respectively) was synthesized using a modified co-thermalysis method.[51,52] Herein we take the procedure of $NaYbF_4$: Yb^{3+}/Tm^{3+} as an example, and the other two were synthesized similarly. Tm_2O_3 (0.025 mmol) and Yb_2O_3 (1.225 mmol) were mixed and then solubilized in 20 mL of 50% aqueous trifluoroacetic acid at 80 °C in a three-neck round-bottom flask. After about 2 h the solution became clear, and then the residual water and acid were slowly evaporated to dryness at 80 °C. Subsequently 5 mL of DI water was added to redissolve the dried white powder. A 4.5 mmol amount of sodium trifluoroacetate was then added to the reaction vessel with 30 mL of octadecene (90%) and 30 mL of oleic acid (90%). The obtained solutions were slowly heated to 140 °C under vacuum with magnetic stirring for 40 min to remove residual water and oxygen, during which time the flask was purged periodically with dry argon gas. After water evaporated, the clear, yellow solution was heated to 320 °C at a rate of about 15 °C per minute under argon gas protection and kept at this temperature under vigorous stirring for about half an hour. Finally the heated solution was gradually cooled to room temperature. The $NaYbF_4$: Yb^{3+}/Tm^{3+} was precipitated by the addition of 100 mL of ethanol and isolated *via* centrifugation at 10 000 rpm. The resulting pellet was then washed twice with mixture of methanol and ethanol (1:1) and isolated *via* centrifugation at 10 000 rpm each time. The resulting muddy nanoparticles were dispersed in cyclohexane or chloroform by sonicating for 5 min for further characterization.

Surface Functionalization of Nanoparticles. The as-synthesized UCNPs were further surface functionalized for bioimaging experiments. Scheme 2 illustrates the process of hydrophilization and coating of hydrophobic OA-capped UCNPs, antibody bioconjugation, and the incubation of anti-CEA8-UCNPs with HeLa cancer cells. A 200 μL amount of $NaYbF_4$:Yb^{3+}/Er^{3+} ($NaYbF_4$:Yb^{3+}/Ho^{3+}) chloroform suspension and 120 mg of MSA were added to a mixture of 2 mL of DI water and 8 mL of chloroform. Then the MSA encapsulation was initiated with the addition of 300 μL of aqueous ammonia (~30%), and the mixture was kept overnight at room temperature under vigorous stirring. Water-dispersible MSA-$NaYbF_4$: Yb^{3+}/Er^{3+} ($NaYbF_4$: Yb^{3+} /Ho^{3+}) nanoparticles were obtained after being washed two times successively with ethanol and DI water. For PAH coating, 200 μL of PAH solution (20 mg/mL in 10 mM NaCl) and 100 μL of 10 mM NaCl solution were added into the prepared MSA-UCNP water solution. This mixed solution was then vortexed vigorously for 3 min. After 3 h adsorption time, the excess PAH molecules in the supernatant fraction were removed by centrifugation twice, and the pellet was redispersed in PBS water. The bioconjugation between the anti-CEA8 and PAH-MSA-UCNPs was realized through noncovalent bonding. A 10 μL portion of anti-CEA8 (0.5 mg/mL) was added to 100 μL of as-prepared PAH-MSA-UCNPs PBS solution and incubated for about 1 h at room temperature. Then anti-CEA8-UCNPs were obtained *via* centrifugation to remove the unconjugated antibody molecules and were redispersed into PBS solution for *in vitro* cell imaging. DSPE-mPEG-5000 was used to directly encapsulate hydrophobic $NaYbF_4$: Yb^{3+}/Tm^{3+} for *in vivo* experiments. Then 1 mL of 25 g/mL DSPE-mPEG-5000 chloroform solution was mixed with 0.2 mL of as-prepared $NaYbF_4$: Yb^{3+}/Tm^{3+} chloroform suspension. The mixture solution was further sonicated 10 min, and then the chloroform was slowly evaporated (while rotating) to dryness at 80 °C under vacuum condition. A 500 μL sample of PBS solution was used to dissolve the DSPE-mPEG-5000-UCNPs.

Instruments. Two power-tunable semiconductor lasers, a 915 nm laser (Shanghai Connet Fiber Optics Co., Ltd.) and a 980 nm laser (Wuhan ZJKC Technology Co., Ltd.), were utilized in the experiments. The size and shape of the nanoparticles were characterized by transmission electron microscopy using a JEOL JEM-1200EX microscope at an acceleration voltage of 160 kV. Zeta potential measurements were performed on a Malvern Zetasizer Nano ZS90 instrument at room temperature. The samples were treated with PBS (pH 7.4) solution before measurement. An X-ray diffractometer (PANalytica X'PERT PRO SUPER) was used to collect the XRD data. A Fourier transform

infrared spectroscope (FTIR, NICOTCT, Thermo Nicolet Corporation, USA) was used to measure the FTIR spectrum of prepared UCNPs. A professional infrared thermal imaging camera (FLIR ThermaCAM S65) was used to record the thermographic maps of laser-irradiated mice. Green and red UC photoluminescence from $NaYbF_4$: Yb^{3+}/Er^{3+} and $NaYbF_4$: Yb^{3+}/Ho^{3+} were obtained using a fluorescence spectrophotometer (F-2500, Hitachi, Japan) with 915 nm laser excitation. Another compact fiber-coupled spectroscope (Ocean Optics, USB2000) was used to measure the spectrum of $NaYbF_4$: Yb^{3+}/Tm^{3+} excited by 915 nm light and the absorption spectra of transparent colloidal UCNPs and black ink solution. Photographic images of UCNP suspensions were taken by a digital camera (Nikon D40, Japan) without adding any filter. The *in vitro* HeLa cancer imaging was completed using a laser confocal scanning microscope (Olympus, FV1000) under CW excitation at 915 nm. *In vivo* experiments were performed in compliance with Zhejiang University Animal Study Committee's requirements for the care and use of laboratory animals in research. A Maestro imaging system (CRI, Inc., Woburn, MA) equipped with 915 and 980 nm lasers was used to perform phantom imaging and *in vivo* mouse imaging.

Acknowledgment. This work was supported by the National Nature Science Foundation of China (No. 60978063 and No. 61008052), the Swedish Foundation for Strategic Research (SSF), the Fundamental Research Funds for the Central Universities, and the China Postdoctoral Science Foundation (20090461394). Q.Z. is grateful to Olympus Company for help in terms of laser scanning confocal microscopy. We also want to express our deepest gratitude toward the Medical School of Zhejiang University for their supply of cells and Prof. Y. Mu's group, Zhejiang Univ., and F. Cai for their help in terms of *in vivo* imaging and phantom imaging experiments.

Supporting Information Available: TEM images of synthesized $NaYbF_4$: Yb^{3+}/Ho^{3+} and $NaYbF_4$: Yb^{3+}/Tm^{3+} and their size diameter distribution; X-ray diffraction patterns of $NaYbF_4$: Yb^{3+}/Er^{3+} UCNPs. FTIR spectrum of OA-capped $NaYbF_4$: Yb^{3+}/Er^{3+} UCNPs, MSA-$NaYbF_4$: Yb^{3+}/Er^{3+}, and PAH-MSA-$NaYbF_4$: Yb^{3+}/Er^{3+}. Optical absorption spectrum of black India ink used in the phantom experiment. This material is available free of charge *via* the Internet at http://pubs.acs.org.

REFERENCES AND NOTES

1. Grunwald, D.; Singer, R. H. *In Vivo* Imaging of Labelled Endogenous Beta-actin mRNA during Nucleocytoplasmic Transport. *Nature* **2010**, *467*, 604–U128.
2. van de Rijke, F.; Zijlmans, H.; Li, S.; Vail, T.; Raap, A. K.; Niedbala, R. S.; Tanke, H. J. Up-converting Phosphor Reporters for Nucleic Acid Microarrays. *Nat. Biotechnol.* **2001**, *19*, 273–276.
3. Prasad, P. N., *Introduction to Biophotonics*; Wiley-Interscience: New York, 2003.
4. Qian, J.; Fu, T.; Zhan, Q. Q.; He, S. L. Using Some Nanoparticles as Contrast Agents for Optical Bioimaging. *IEEE J. Sel. Top. Quant.* **2010**, *16*, 672–684.
5. Prasad, P. N. *Nanophotonics*; Wiley-Interscience: New York, 2004.
6. Chen, Z. G.; Chen, H. L.; Hu, H.; Yu, M. X.; Li, F. Y.; Zhang, Q.; Zhou, Z. G.; Yi, T.; Huang, C. H. Versatile Synthesis Strategy for Carboxylic Acid-Functionalized Upconverting Nanophosphors as Biological Labels. *J. Am. Chem. Soc.* **2008**, *130*, 3023–3029.
7. Thilwind, R. E.; 't Hooft, G.; Uzunbajakava, N. E. Improved Depth Resolution in Near-infrared Diffuse Reflectance Spectroscopy Using Obliquely Oriented Fibers. *J. Biomed. Opt.* **2009**, *14*, 024026.
8. Lenz, P. Fluorescence Measurement in Thick Tissue Layers by Linear or Nonlinear Long-Wavelength Excitation. *Appl. Opt.* **1999**, *38*, 3662–3669.
9. Qian, J.; Jiang, L.; Cai, F.; Wang, D.; He, S. Fluorescence-surface Enhanced Raman Scattering Co-functionalized Gold Nanorods as Near-infrared Probes for Purely Optical *in Vivo* Imaging. *Biomaterials* **2011**, *32*, 1601–1610.
10. Kumar, R.; Roy, I.; Ohulchanskky, T. Y.; Vathy, L. A.; Bergey, E. J.; Sajjad, M.; Prasad, P. N. *In Vivo* Biodistribution and Clearance Studies Using Multimodal Organically Modified Silica Nanoparticles. *ACS Nano* **2010**, *4*, 699–708.
11. Resch-Genger, U.; Grabolle, M.; Cavaliere-Jaricot, S.; Nitschke, R.; Nann, T. Quantum Dots versus Organic Dyes as Fluorescent Labels. *Nat. Methods* **2008**, *5*, 763–775.
12. Alivisatos, A. P. Semiconductor Clusters, Nanocrystals, and Quantum Dots. *Science* **1996**, *271*, 933–937.
13. Eggeling, C.; Widengren, J.; Rigler, R.; Seidel, C. A. M. Photobleaching of Fluorescent Dyes under Conditions Used for Single-Molecule Detection: Evidence of Two-Step Photolysis. *Anal. Chem.* **1998**, *70*, 2651–2659.
14. Deng, Z. T.; Schulz, O.; Lin, S.; Ding, B. Q.; Liu, X. W.; Wei, X. X.; Ros, R.; Yan, H.; Liu, Y. Aqueous Synthesis of Zinc Blende CdTe/CdS Magic-Core/Thick-Shell Tetrahedral-Shaped Nanocrystals with Emission Tunable to Near-Infrared. *J. Am. Chem. Soc.* **2010**, *132*, 5592.
15. Kim, S.; Lim, Y. T.; Soltesz, E. G.; De Grand, A. M.; Lee, J.; Nakayama, A.; Parker, J. A.; Mihaljevic, T.; Laurence, R. G.; Dor, D. M.; *et al*. Near-infrared Fluorescent Type II Quantum Dots for Sentinel Lymph Node Mapping. *Nat. Biotechnol.* **2004**, *22*, 93–97.
16. Shiohara, A.; Hoshino, A.; Hanaki, K.; Suzuki, K.; Yamamoto, K. On the Cyto-toxicity Caused by Quantum Dots. *Microbiol. Immunol.* **2004**, *48*, 669–675.
17. Derfus, A. M.; Chan, W. C. W.; Bhatia, S. N. Probing the Cytotoxicity of Semiconductor Quantum Dots. *Nano Lett.* **2004**, *4*, 11–18.
18. Wang, F.; Liu, X. G. Recent Advances in the Chemistry of Lanthanide-doped Upconversion Nanocrystals. *Chem. Soc. Rev.* **2009**, *38*, 976–989.
19. Xiong, L.; Chen, Z.; Tian, Q.; Cao, T.; Xu, C.; Li, F. High Contrast Upconversion Luminescence Targeted Imaging *in Vivo* Using Peptide-Labeled Nanophosphors. *Anal. Chem.* **2009**, *81*, 8687–8694.
20. Wang, M.; Mi, C. C.; Wang, W. X.; Liu, C. H.; Wu, Y. F.; Xu, Z. R.; Mao, C. B.; Xu, S. K. Immunolabeling and NIR-Excited Fluorescent Imaging of HeLa Cells by Using NaYF4:Yb,Er Upconversion Nanoparticles. *ACS Nano* **2009**, *3*, 1580–1586.
21. Hu, H.; Xiong, L. Q.; Zhou, J.; Li, F. Y.; Cao, T. Y.; Huang, C. H. Multimodal-Luminescence Core-Shell Nanocomposites for Targeted Imaging of Tumor Cells. *Chem.—Eur. J.* **2009**, *15*, 3577–3584.
22. Xiong, L. Q.; Yang, T. S.; Yang, Y.; Xu, C. J.; Li, F. Y. Long-term *in Vivo* Biodistribution Imaging and Toxicity of Polyacrylic Acid-coated Upconversion Nanophosphors. *Biomaterials* **2010**, *31*, 7078–7085.
23. Nyk, M.; Kumar, R.; Ohulchanskyy, T. Y.; Bergey, E. J.; Prasad, P. N. High Contrast *in Vitro* and *in Vivo* Photoluminescence Bioimaging Using Near Infrared to Near Infrared Up-Conversion in Tm^{3+} and Yb^{3+} Doped Fluoride Nanophosphors. *Nano Lett.* **2008**, *8*, 3834–3838.
24. Zhou, J.; Yu, M. X.; Sun, Y.; Zhang, X. Z.; Zhu, X. J.; Wu, Z. H.; Wu, D. M.; Li, F. Y. Fluorine-18-labeled $Gd^{3+}/Yb^{3+}/Er^{3+}$ Co-doped $NaYF_4$ Nanophosphors for Multimodality PET/MR/UCL Imaging. *Biomaterials* **2011**, *32*, 1148–1156.
25. Sun, Y.; Yu, M. X.; Liang, S.; Zhang, Y. J.; Li, C. G.; Mou, T. T.; Yang, W. J.; Zhang, X. Z.; Li, B. A.; Huang, C. H.; Li, F. Y. Fluorine-18 Labeled Rare-earth Nanoparticles for Positron Emission Tomography (PET) Imaging of Sentinel Lymph Node. *Biomaterials* **2011**, *32*, 2999–3007.
26. Liu, Q.; Sun, Y.; Li, C.; Zhou, J.; Li, C.; Yang, T.; Zhang, X.; Yi, T.; Wu, D.; Li, F. ^{18}F-Labeled Magnetic-Upconversion Nanophosphors *via* Rare-Earth Cation-Assisted Ligand Assembly. *ACS Nano* 2011, in press (online available).
27. Kumar, M.; Zhang, P. Highly Sensitive and Selective Label-Free Optical Detection of DNA Hybridization Based on Photon Upconverting Nanoparticles. *Langmuir* **2009**, *25*, 6024–6027.
28. Kumar, M.; Zhang, P. Highly Sensitive and Selective Label-free Optical Detection of Mercuric ions Using Photon Upconverting Nanoparticles. *Biosens. Bioelectron.* **2010**, *25*, 2431–2435.

29. Guo, H. C.; Qian, H. S.; Idris, N. M.; Zhang, Y. Singlet Oxygen-Induced Apoptosis of Cancer Cells Using Upconversion Fluorescent Nanoparticles as A Carrier of Photosensitizer. *Nanomed. Nanotechnol.* **2010**, *6*, 486–495.
30. Ungun, B.; Prud'homme, R. K.; Budijono, S. J.; Shan, J. N.; Lim, S. F.; Ju, Y. G.; Austin, R. Nanofabricated Upconversion Nanoparticles for Photodynamic Therapy. *Opt. Express* **2009**, *17*, 80–86.
31. Liu, H. C.; Xu, C. T.; Andersson-Engels, S. Multibeam Fluorescence Diffuse Optical Tomography Using Upconverting Nanoparticles. *Opt. Lett.* **2010**, *35*, 718–720.
32. Xu, C. T.; Axelsson, J.; Andersson-Engels, S. Fluorescence Diffuse Optical Tomography Using Upconverting Nanoparticles. *Appl. Phys. Lett.* **2009**, *94*, 251107.
33. Kou, L. H.; Labrie, D.; Chylek, P. Refractive-Indexes of Water and Ice in the 0.65-Mu-M to 2.5-Mu-M Spectral Range. *Appl. Opt.* **1993**, *32*, 3531–3540.
34. Kangasniemi, M.; McNichols, R. J.; Bankson, J. A.; Gowda, A.; Price, R. E.; Hazle, J. D. Thermal Therapy of Canine Cerebral Tumors Using a 980 nm Diode Laser with MR Temperature-sensitive Imaging Feedback. *Laser Surg. Med.* **2004**, *35*, 41–50.
35. Tabakoglu, H. O.; Topaloglu, N.; Gulsoy, M. The Effect of Irradiance Level in 980-nm Diode Laser Skin Welding. *Photomed. Laser Surg.* **2010**, *28*, 453–458.
36. Reynaud, J. P.; Skibinski, M.; Wassmer, B.; Rochon, P.; Mordon, S. Lipolysis Using a 980-nm Diode Laser: A Retrospective Analysis of 534 Procedures. *Aesthet. Plast. Surg.* **2009**, *33*, 28–36.
37. Chen, G. Y.; Ohulchanskyy, T. Y.; Kumar, R.; Agren, H.; Prasad, P. N. Ultrasmall Monodisperse $NaYF_4$:Yb^{3+}/Tm^{3+} Nanocrystals with Enhanced Near-Infrared to Near-Infrared Upconversion Photoluminescence. *ACS Nano* **2010**, *4*, 3163–3168.
38. Ko, A.; Rosenbaum, E. H.; Dollinger, M. Everyone's Guide to Cancer Therapy: How Cancer Is Diagnosed, Treated, and Managed Day to Day, Revised 5th ed.; Andrews McMeel Publishing: Kansas City, 2008; pp 98−100.
39. Freeman, C.; Halperin, E. C. B., Luther, W.; Wazer, D. E. *Perez and Brady's Principles and Practice of Radiation Oncology*; Wolters Kluwer Health/Lippincott Williams & Wilkins: Philadelphia, 2008; pp 637−644.
40. Chen, C. L.; Kuo, L. R.; Chang, C. L.; Hwu, Y. K.; Huang, C. K.; Lee, S. Y.; Chen, K.; Lin, S. J.; Huang, J. D.; Chen, Y. Y. In Situ Real-time Investigation of Cancer Cell Photothermolysis Mediated by Excited Gold Nanorod Surface Plasmons. *Biomaterials* **2010**, *31*, 4104–4112.
41. Svenmarker, P.; Xu, C. T.; Andersson-Engels, S. Use of Nonlinear Upconverting Nanoparticles Provides Increased Spatial Resolution in Fluorescence Diffuse Imaging. *Opt. Lett.* **2010**, *35*, 2789–2791.
42. Xiong, L. Q.; Chen, Z. G.; Yu, M. X.; Li, F. Y.; Liu, C.; Huang, C. H. Synthesis, Characterization, and in Vivo Targeted Imaging of Amine-functionalized Rare-earth Up-converting Nanophosphors. *Biomaterials* **2009**, *30*, 5592–5600.
43. Zhou, J.; Sun, Y.; Du, X. X.; Xiong, L. Q.; Hu, H.; Li, F. Y. Dual-modality *in Vivo* Imaging Using Rare-earth Nanocrystals with Near-infrared to Near-infrared (NIR-to-NIR) Upconversion Luminescence and Magnetic Resonance Properties. *Biomaterials* **2010**, *31*, 3287–3295.
44. Tian, Z.; Chen, G. Y.; Li, X.; Liang, H. J.; Li, Y. S.; Zhang, Z. G.; Tian, Y. Autofluorescence-free *in Vivo* Multicolor Imaging Using Upconversion Fluoride Nanocrystals. *Laser Med. Sci.* **2010**, *25*, 479–484.
45. Alexandrakis, G.; Rannou, F. R.; Chatziioannou, A. F. Tomographic Bioluminescence Imaging by Use of a Combined Optical-PET (OPET) System: a Computer Simulation Feasibility Study. *Phys. Med. Biol.* **2005**, *50*, 4225–4241.
46. Crochet, J. J.; Gnyawali, S. C.; Chen, Y. C.; Lemley, E. C.; Wang, L. H. V.; Chen, W. R. Temperature Distribution in Selective Laser-tissue Interaction. *J. Biomed. Opt.* **2006**, *11*, 034031.
47. Liemert, A.; Kienle, A. Light Diffusion in a Turbid Cylinder. I. Homogeneous Case. *Opt. Express* **2010**, *18*, 9456–9473.
48. Arridge, S. R. Optical Tomography in Medical Imaging. *Inverse Probl.* **1999**, *15*, R41–R93.
49. Vinegoni, C.; Razansky, D.; Hilderbrand, S. A.; Shao, F. W.; Ntziachristos, V.; Weissleder, R. Transillumination Fluorescence Imaging in Mice Using Biocompatible Upconverting Nanoparticles. *Opt. Lett.* **2009**, *34*, 2566–2568.
50. Xu, C. T.; Svensson, N.; Axelsson, J.; Svenmarker, P.; Somesfalean, G.; Chen, G. Y.; Liang, H. J.; Liu, H. C.; Zhang, Z. G.; Andersson-Engels, S. Autofluorescence Insensitive Imaging Using Upconverting Nanocrystals in Scattering Media. *Appl. Phys. Lett.* **2008**, *93*, 171103.
51. Boyer, J. C.; Vetrone, F.; Cuccia, L. A.; Capobianco, J. A. Synthesis of Colloidal Upconverting $NaYF_4$ Nanocrystals Doped with Er^{3+}, Yb^{3+} and Tm^{3+}, Yb^{3+} *via* Thermal Decomposition of Lanthanide Trifluoroacetate Precursors. *J. Am. Chem. Soc.* **2006**, *128*, 7444–7445.
52. Boyer, J. C.; Cuccia, L. A.; Capobianco, J. A. Synthesis of Colloidal Upconverting $NaYF_4$: Er^{3+}/Yb^{3+} and Tm^{3+}/Yb^{3+} Monodisperse Nanocrystals. *Nano Lett.* **2007**, *7*, 847–852.
53. Zhan, Q. Q.; Qian, J.; Li, X.; He, S. L. A Study of Mesoporous Silica-encapsulated Gold Nanorods as Enhanced Light Scattering Probes for Cancer Cell Imaging. *Nanotechnology* **2010**, *21*, 055704.
54. Keijzer, M.; Star, W. M.; Storchi, P. R. M. Optical Diffusion in Layered Media. *Appl. Opt.* **1988**, *27*, 1820–1824.
55. Oregon Medical Laser Center of Oregon Health and Sciences University. http://omlc.ogi.edu/spectra/.